

# Localisation of optimal perturbations in variable viscosity channel flow

Sharath Jose<sup>\*,a</sup>, Luca Brandt<sup>b</sup>, Rama Govindarajan<sup>c</sup>

<sup>a</sup> Department of Aerospace Engineering, Indian Institute of Technology Madras, Chennai, India

<sup>b</sup> Linné Flow Centre and Swedish e-Science Research Centre, KTH Mechanics, Stockholm 100 44, Sweden

<sup>c</sup> International Centre for Theoretical Sciences (ICTS-TIFR) Shivakote, Hesarghatta Hobli, Bengaluru 560089, India

## ARTICLE INFO

### Keywords:

Nonmodal stability  
Variable viscosity  
Localised optimal perturbations

## ABSTRACT

We discuss how a variable fluid viscosity affects the nonmodal stability characteristics of the pressure driven flow between two parallel walls maintained at different temperatures. In this work, we specify the fluid viscosity to be a function of the fluid temperature. We employ an Arrhenius model to model the viscosity of water, and Sutherland's law to model the viscosity of air. We impose a stable density stratification, and find that strong density stratification can suppress optimal transient growth regardless of how strong the viscosity variation is. Some studies have been inclined to neglect viscosity stratification, since the changes in *levels* of optimal growth, when compared to the uniform viscosity case, are often not too significant. In this article, we show significant localisation of optimal perturbation energy in the less viscous region, a feature that is not observed in uniform viscosity flows. This can have a bearing on the route to turbulence in these systems.

## 1. Introduction

Flows involving fluids with variable viscosity are commonly encountered in a wide range of scenarios that are of fundamental and applied interests. The fluid viscosity being non-uniform may be due to factors such as temperature, pressure and composition; such conditions are frequently observed in chemical, food and petroleum industries. For issues of practical interest such as drag reduction, heat transfer, and turbulent mixing, varying fluid properties may imply vastly differing characteristics than from the case with a homogeneous fluid (Gad-el-Hak, 2001; White and Mungal, 2008). It has been shown that the skin friction coefficient and drag reduce, and heat transfer increases when temperature dependent viscosity is considered (Lee et al., 2013; 2014). The need for a more inclusive analysis has gained relevance recently as it has been shown that the mean flow quantities are altered in turbulent flows due to variations in viscosity (for e.g. see Zonta et al., 2012a; 2012b; Talbot et al., 2013; Taguelmimt et al., 2016). These studies suggest that the effect of viscosity is not necessarily limited only to the smallest scales of motion (Voivenel et al., 2016). Thus consequences of such results find relevance in turbulent modelling (Zonta, 2013; Pecnik and Patel, 2017).

The work of Yih (1967) was among the earliest to investigate exponentially growing modal instabilities in a plane shear flow when the viscosity of the fluid is not uniform. When the fluid viscosity is a function of space, it may either promote stabilisation or destabilisation

of the system (Ranganathan and Govindarajan, 2001; Govindarajan et al., 2001). In certain cases, viscosity stratification may leave the stability characteristics unchanged. Variations in viscosity (and fluid properties) are commonly encountered in systems involving non-Newtonian fluid flow and multiphase flow. The review by Govindarajan and Sahu (2014) describes a wide range of instabilities in the systems with varying viscosity, and emphasises that the nature of the viscosity stratification is crucial to determine the instability characteristics.

It has been established that nonmodal mechanisms play a pivotal role in the transition to turbulence in parallel shear flows (Schmid and Henningson, 2001; Schmid, 2007). From modal stability analysis, we can accurately predict the asymptotic behaviour of disturbances at long times. However, as the linear system is non-self adjoint, and therefore the eigenfunctions of the linearised system are nonnormal, initial perturbations can grow transiently even when the system does not support any exponential instabilities. The transient growth can be large enough such that nonlinear effects can no longer be neglected and the flow might become turbulent. Earlier studies on shear flows with variable viscosity report that the optimal transient growth does not change drastically, with mild stabilisation/destabilisation observed (Chikkadi et al., 2005; Nouar et al., 2007; Ren et al., 2019; Sameen and Govindarajan, 2007). Based on these results, it is tempting to conclude the effect of viscosity stratification for nonmodal dynamics to be not very significant. However an analysis of a viscosity stratified flow based on a volume-averaged quantity like the optimal transient growth does

\* Corresponding author.

E-mail addresses: [sharath872000@gmail.com](mailto:sharath872000@gmail.com) (S. Jose), [luca@mech.kth.se](mailto:luca@mech.kth.se) (L. Brandt), [rama@icts.res.in](mailto:rama@icts.res.in) (R. Govindarajan).

not necessarily provide a full picture as the optimal perturbations themselves may be considerably different.

In this article, we consider nonmodal stability characteristics of a parallel flow of a fluid with temperature dependent viscosity through a channel with walls maintained at different temperatures. This configuration is one of the systems investigated by Sameen and Govindarajan (2007), where they examined changes in characteristics of modal stability, secondary instabilities and nonmodal stability as the system parameters are varied (see also Sameen et al., 2011). Here, our main focus is on the spatial structure of the optimal perturbation, which has not been examined in the earlier studies mentioned above. We are interested in the distribution of the perturbation energy in the channel, and how it evolves in time. With variable viscosity, we find the optimal structures to be strongly localised in the less viscous region of the channel.

The layout of the paper is as follows. The system under consideration is described in Section 2, and this is followed by a discussion of the problem formulation in Section 3. The results of this study are then presented in Sections 4 and 5. In Section 6, we summarise the results and offer some concluding statements.

## 2. Description of system

### 2.1. Flow configuration

In this study, we examine the pressure driven flow between two parallel walls of a fluid whose viscosity is dependent on the fluid temperature. The walls are assumed to extend indefinitely along the streamwise  $x$  and spanwise  $z$  coordinates, and are maintained at fixed temperatures  $T_l$  (lower wall) and  $T_u$  (upper wall). The distance between the two walls is  $2d$ , and we specify the wall-normal coordinate  $y$  to be zero at the channel centreline. When the temperature difference  $\Delta T \equiv T_u - T_l$  is non-zero, effects of variable viscosity come into play. We fix  $T_l = 295$  K, and use  $\Delta T$  to specify the extent of the viscosity stratification. Gravity acts along the negative  $y$  coordinate. The flow configuration is depicted schematically in Fig. 1.

### 2.2. Governing equations

The nondimensional governing equations for the system, using the Boussinesq approximation, are as follows:

$$\partial_i u_i + u_j \partial_j u_i = -\partial_i p + Ri T \delta_{i2} + \frac{1}{Re} \partial_j [\mu (\partial_j u_i + \partial_i u_j)], \quad (1)$$

$$\partial_j u_j = 0, \quad (2)$$

$$\partial_i T + u_j \partial_j T = \frac{1}{Re Pr} \partial_j \partial_j T. \quad (3)$$

Above,  $u_i$  is the Eulerian velocity,  $\mu$  is the viscosity,  $T$  is the temperature and  $p$  is the pressure. The nondimensional parameters that characterise the flow are the Reynolds number  $Re \equiv \rho_0 U_0 d / \mu_0$ , the Prandtl number

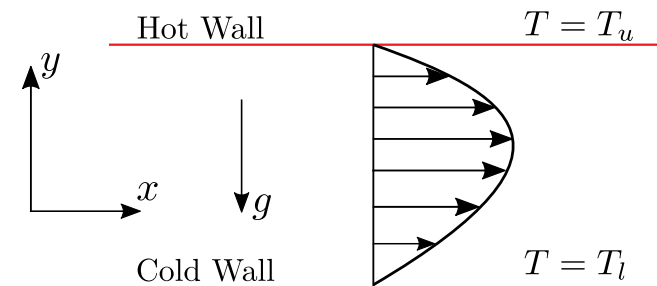


Fig. 1. Base flow configuration: Fully developed flow between two infinitely extending parallel plates, separated by a distance  $2d$ , and maintained at different temperatures.

$Pr \equiv \mu_0 / \rho_0 \kappa$  and the Richardson number  $Ri \equiv \gamma g \Delta T d / U_0^2$ . Given a fluid,  $\rho_0$  is the reference density,  $\kappa$  the thermal diffusivity,  $\gamma$  the thermal expansion coefficient and  $\mu_0$  the reference viscosity.  $g$  is the acceleration due to gravity and  $U_0$  is the reference velocity scale, defined in the following subsection in terms of bulk velocity. The channel half-width  $d$  is the reference length scale; after nondimensionalisation, we have  $y \in [-1, 1]$  with the walls located at  $y = \pm 1$ .

### 2.3. Steady laminar base flow

For the steady base state, the dimensional temperature  $\bar{T}_d$  varies linearly between the two walls, i.e.  $\bar{T}_d = T_l + 0.5 \Delta T (y + 1)$ . Using  $\Delta T$  as the reference scale for nondimensionalising temperature variables, we obtain the nondimensional mean temperature as  $\bar{T} = 0.5(y + 1)$ . In the present study, non-zero values of  $\Delta T$  imply that variable fluid viscosity is considered for a given case. To be able to distinctly account for temperature effects due to gravity, the Richardson number  $Ri$  is used. In this study, therefore, it is emphasised that  $\Delta T = 0$  K only implies that viscosity is constant across the channel. The steady state viscosity profile  $\bar{\mu}_d$  is found using  $\bar{T}_d$ ; in this study, we use an Arrhenius model and Sutherland's law to model the viscosity of water and air respectively. For fair comparison, we choose  $\mu_0$  to be the average viscosity across the channel. The nondimensional base state viscosity profile is then given by:

$$\bar{\mu} = \frac{\bar{\mu}_d}{\mu_0}. \quad (4)$$

Under steady state conditions, the flow is unidirectional along the positive  $x$  direction with a velocity profile  $U$  that is a function of the wall-normal coordinate  $y$  alone. When the fluid viscosity is not constant, the steady base flow is obtained by solving the streamwise momentum equation:

$$0 = -\mathcal{G} + \frac{d}{dy} \left( \bar{\mu} \frac{dU}{dy} \right), \quad (5)$$

where  $\mathcal{G}$  is the nondimensional mean pressure gradient in the streamwise direction. Note that there is also a hydrostatic pressure due to the mean temperature gradient. The flow obeys no-slip conditions at the walls, i.e.,  $U(\pm 1) = 0$ . As the viscosity is not constant, the maximum velocity in the flow  $U_m$  occurs away from the channel centreline at  $y = y_m$ . Using these conditions, we get the expressions for  $y_m$  and  $U$  as follows:

$$y_m = \frac{I_2}{I_1}, \quad (6)$$

$$U(y) = \frac{U_m}{I_1 I_2' - I_2 I_1'} \left[ I_1 \int_{-1}^y dy' \frac{y'}{\bar{\mu}(y')} - I_2 \int_{-1}^y dy' \frac{1}{\bar{\mu}(y')} \right], \quad (7)$$

where

$$I_1 = \int_{-1}^1 dy' \frac{1}{\bar{\mu}(y')}, \quad I_2 = \int_{-1}^1 dy' \frac{y'}{\bar{\mu}(y')}, \quad I_1' = \int_{-1}^{y_m} dy' \frac{1}{\bar{\mu}(y')}, \text{ and}$$

$$I_2' = \int_{-1}^{y_m} dy' \frac{y'}{\bar{\mu}(y')}.$$

The details of the derivation of the expressions above are given in Appendix A.

The average velocity is  $2U_m/3$  for a plane Poiseuille flow with a uniform fluid. To ensure fair comparison between the cases with viscosity stratification, we specify the base flows to have the same average velocity. As a result, the reference velocity scale  $U_0$  is defined as:

$$U_0 = \frac{2U_m}{3} \left( \frac{1}{2} \int_{-1}^1 dy' \frac{U(y')}{U_m} \right)^{-1}. \quad (8)$$

The definitions of  $Re$  and  $Ri$  are based on  $U_0$ . By choosing  $U_0$  and  $\mu_0$  as the reference scales, we ensure that the bulk Reynolds number  $Re_b$  is

constant for different viscosity stratifications. Subsequently, we have  $Re_b = 4Re/3$ , as it would be for the constant viscosity case. The steady flow about which we perturb the system, employing expressions in Eqs. (7) and (8), is then given by:

$$\bar{U} = \frac{U}{U_0}. \tag{9}$$

### 3. Problem formulation

#### 3.1. Perturbation equations

To examine the stability of the base state  $\bar{F}$ , we perturb the system such that it is of the form  $f(x, y, z, t) = \bar{F}(y) + f'(x, y, z, t)$ . The mean and the perturbed flows both obey the governing equations given by Eqs. (1)–(3). The evolution equations for the perturbation are obtained by subtracting the equations for the base flow from those of the perturbed flow. Further, we assume the perturbations are to be infinitesimally small when compared with base flow quantities, and the terms that are quadratic in the perturbation quantities are neglected to yield a linearised set of equations. The fluid temperature perturbation  $\theta'$  is governed by a linearised advection-diffusion equation. For the viscosity perturbation  $\mu'$ , we relate it to  $\theta'$  results using a Taylor's expansion about the mean temperature  $\bar{T}$ . In the linear limit, we have

$$\mu' = \frac{\partial \bar{\mu}}{\partial T} \theta'. \tag{10}$$

For parallel shear flows, the linearised momentum equation and continuity equation can be recast as the Orr–Sommerfeld–Squire set of equations to eliminate the pressure (Drazin and Reid, 2004). In this study, we work with a generalised Orr–Sommerfeld–Squire set of equations that account for viscosity and density stratifications. Assuming periodicity in the homogeneous directions, the perturbation dynamics can be analysed in Fourier space, with  $\alpha$  the streamwise wavenumber and  $\beta$  the spanwise wavenumber; the disturbances take hence the form  $f'(x, y, z, t) = \hat{f}(y, t)e^{i(\alpha x + \beta z)}$ . Then the linearised equations governing the disturbance evolution can be written in a simplified block form as follows:

$$\frac{\partial}{\partial t} \begin{bmatrix} \Delta & 0 & 0 \\ 0 & 1 & 0 \\ 0 & 0 & 1 \end{bmatrix} \begin{bmatrix} \hat{v} \\ \hat{\eta} \\ \hat{\theta} \end{bmatrix} = \begin{bmatrix} L_{\hat{v}\hat{v}} & 0 & L_{\hat{v}\hat{\theta}} \\ L_{\hat{\eta}\hat{v}} & L_{\hat{\eta}\hat{\eta}} & L_{\hat{\eta}\hat{\theta}} \\ L_{\hat{\theta}\hat{v}} & 0 & L_{\hat{\theta}\hat{\theta}} \end{bmatrix} \begin{bmatrix} \hat{v} \\ \hat{\eta} \\ \hat{\theta} \end{bmatrix} \tag{11}$$

Above, the state vector defining the perturbation is  $\hat{\mathbf{q}} = [\hat{v} \ \hat{\eta} \ \hat{\theta}]^T$ ;  $\hat{v}$  and  $\hat{\eta}$  are the normal components of the perturbation velocity and vorticity respectively. In addition, note that  $\Delta = D^2 - k^2$  with  $D = \partial/\partial y$  and  $k^2 = \alpha^2 + \beta^2$ . The different operators are defined below.

$$\begin{aligned} L_{\hat{v}\hat{v}} &= \frac{1}{Re} [\bar{\mu} \Delta^2 + 2\bar{\mu}' \Delta D + \bar{\mu}'' \Delta + 2k^2 \bar{\mu}'] - i\alpha \bar{U} \Delta + i\alpha \bar{U}'' \\ L_{\hat{\eta}\hat{v}} &= -\frac{i\alpha}{Re} \{ \bar{U}' \Delta + 2k^2 \bar{U}' + 2\bar{U}'' D + \bar{U}''' \} \frac{d\bar{\mu}}{dT} - k^2 Ri \\ L_{\hat{\eta}\hat{\eta}} &= -i\beta \bar{U}' \\ L_{\hat{\eta}\hat{\theta}} &= -i\alpha \bar{U} + \frac{1}{Re} \{ \bar{\mu}' D + \bar{\mu} (D^2 - k^2) \} \\ L_{\hat{\theta}\hat{v}} &= \frac{i\beta}{Re} \{ \bar{U}'' + \bar{U}' D \} \frac{d\bar{\mu}}{dT} \\ L_{\hat{\theta}\hat{\eta}} &= -\bar{T}' \\ L_{\hat{\theta}\hat{\theta}} &= -i\alpha \bar{U} + \frac{1}{Re Pr} (D^2 - k^2). \end{aligned}$$

In the operators shown above, the primes denote derivatives with respect to normal coordinate  $y$ . These operators define the forcing due to different components of the state vector. At the wall, where the flow obeys no slip condition with constant fluid temperature, the different components of the state vector are subject to the following boundary

conditions:

$$\begin{aligned} \hat{v}(\pm 1, t) &= D\hat{v}(\pm 1, t) = 0, \\ \hat{\eta}(\pm 1, t) &= \hat{\theta}(\pm 1, t) = 0, \quad t \geq 0 \end{aligned} \tag{12}$$

When viscosity stratification is neglected,  $L_{\hat{v}\hat{v}}$  and  $L_{\hat{\eta}\hat{\eta}}$  reduce to the Orr–Sommerfeld and Squire operators respectively (Drazin and Reid, 2004); furthermore,  $L_{\hat{\eta}\hat{v}} = 0$  and  $L_{\hat{\theta}\hat{\theta}} = -k^2 Ri$  when  $\bar{\mu} = 1$ . In the terms involving the mean viscosity  $\bar{\mu}$  and its derivatives, one can immediately see that the choice of reference viscosity plays an important role in defining the linearised operator. Therefore the choice of the average viscosity in the channel as the reference viscosity is most appropriate for purposes of comparisons between different mean temperature gradients. Likewise, fixing the mass flow rate also serves towards ensuring a fair comparison between different cases investigated.

If the perturbation is assumed to evolve in time as  $\hat{f}(y, t) = \tilde{f}(y)e^{-i\omega t}$ , an eigenvalue problem can be formulated from Eq. (11); the eigenvalue  $\omega$  is the complex temporal frequency. There exists an exponential modal instability if there exists an eigenvalue whose imaginary part is greater than zero, i.e.,  $\omega_i > 0$ . The unstable mode grows exponentially until the nonlinear terms become important, and subsequently causes transition of the flow to a new state. For the case where the viscosity is defined by the Arrhenius model, the modal stability characteristics have been discussed in detail by Sameen and Govindarajan (2007).

#### 3.2. Nonmodal stability analysis

In parallel shear flows, transition can occur due to small perturbations even when there exist no exponential instabilities for the prescribed values of the governing parameters (Schmid and Henningson, 2001; Schmid, 2007). The linearised operator in equation (11) is non-normal, as a consequence of which perturbations can exhibit transient algebraic growth. These perturbations depicting transient behaviour are a combination of multiple nonnormal eigenfunctions of the linearised operator. The growth can be strong enough such that the perturbation evolution is no longer linear, and the flow has transitioned to a new state. Nonmodal stability analysis characterises the transient behaviour of perturbations while solving Eq. (11) as an initial value problem.

To quantify the transient behaviour, a choice must be made for an objective functional, based on which optimal perturbations can be evaluated. We choose the gain in terms of the total perturbation energy  $G$  as the objective functional to be maximised for the nonmodal analysis, defined as follows:

$$G = \frac{E(k_x, k_y; t)}{E(k_x, k_y; 0)}. \tag{13}$$

Above,  $E$  gives the total energy of the perturbation with both kinetic and potential contributions (Kaminski et al., 2014), which is of the form given below.

$$E = \frac{1}{8k^2} \int_{-1}^1 (k^2 \hat{v}^* \hat{v} + D\hat{v}^* D\hat{v} + \hat{\eta}^* \hat{\eta} + Ri k^2 \hat{\theta}^* \hat{\theta}) dy. \tag{14}$$

The potential energy of the perturbation is due to  $\hat{\theta}$  and depends on the strength of the background stratification. For a given set of parameters, the global optimal perturbation is the initial condition leading to the largest amplification  $G_{max}$ , when considered over all wavenumbers and time. The time when this transient growth is obtained is called the optimal time  $T_{opt}$ . The wavenumbers defining the optimal perturbation are denoted as  $\alpha_{opt}$  and  $\beta_{opt}$ .

#### 3.3. Numerical methods and validation

For discretisation along the wall-normal coordinate  $y$ , we use a Chebyshev collocation method with 81 Chebyshev polynomials (Weideman and Reddy, 2000). Higher resolutions did not change the

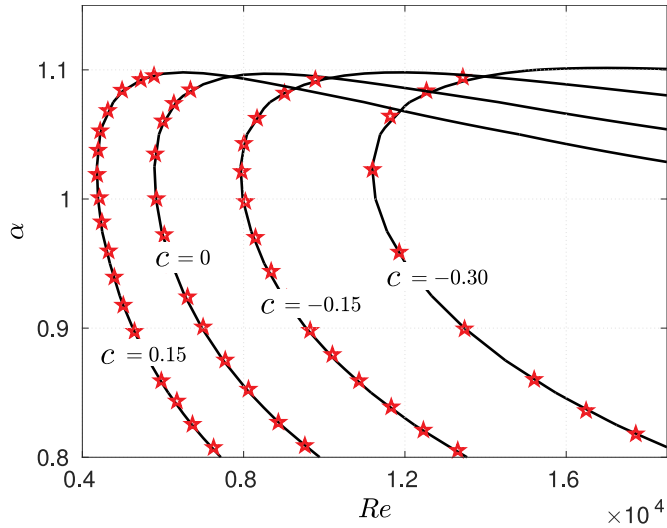


Fig. 2. Validation of code: Viscosity given by  $\mu(T) = \exp(-cT)$ , and  $Ri = 0$ . Solid line (black): present study, stars (red): data from Wall and Wilson (1996). (Colour in online version)

answer to at least 8 decimal places. We evaluate the optimal gains by the singular value decomposition method (Schmid and Brandt, 2014). Upon turning off the viscosity stratification and setting  $Ri = 0$ , we recover the eigenspectra for the plane Poiseuille flow (Appendix A.7 in Schmid and Henningson, 2001). The spectrum for the density stratified channel flow is recovered when  $\Delta T$  alone is set to zero. To validate that the code incorporates viscosity variations faithfully, we have reproduced the stability boundaries obtained by Wall and Wilson (1996) in Fig. 2. In their work, the effect of gravity is not considered, i.e.  $Ri = 0$ .

#### 4. Viscosity stratification in water

In this section, we first employ an Arrhenius law to model the viscosity of water:

$$\bar{\mu}_d = C_1 e^{C_2/\bar{T}_d}, \quad (15)$$

where  $C_1 = 0.00183 \text{ Nsm}^{-2}$  and  $C_2 = 1879.9 \text{ K}$ . For all the results, we select the reference Reynolds number to be 2000; this gives us  $Re_b = 2666.67$  for the full channel. The results do not change qualitatively for other values of  $Re$ . As would be appropriate when the fluid is water, we fix the Prandtl number  $Pr = 7$ . For the range of parameters considered, exponentially growing instabilities are absent.

The nondimensionalised viscosity profiles ( $\bar{\mu}$ ) and the corresponding mean velocity profiles ( $\bar{U}$ ) are evaluated using Eqs. (4) and (9) respectively;  $\bar{\mu}$  and  $\bar{U}$  are shown in Fig. 3 for different temperature gradients. A notable feature in the profiles is that viscosity stratification leads to a greater mass flux in the less viscous half of the channel. This suggests that the effective bulk Reynolds number, defined by average values of velocity and viscosity, in each half would be different. For instance, when  $\Delta T = 25 \text{ K}$ , the effective bulk Reynolds number is 3233.51 and 2224.83 for the upper and lower channel halves respectively. In the following subsections, we examine how this contrast is reflected in the optimal perturbation characteristics.

##### 4.1. Nonmodal stability characteristics

While varying  $Ri$  over a range of values spanning a few decades, the optimal perturbations are evaluated for different values of  $\Delta T$ . To highlight the effect of viscosity stratification, we choose three representative values of the dimensional temperature gradient  $\Delta T = 0 \text{ K}$ ,  $10 \text{ K}$  and  $25 \text{ K}$ . Although we have performed calculations with a larger

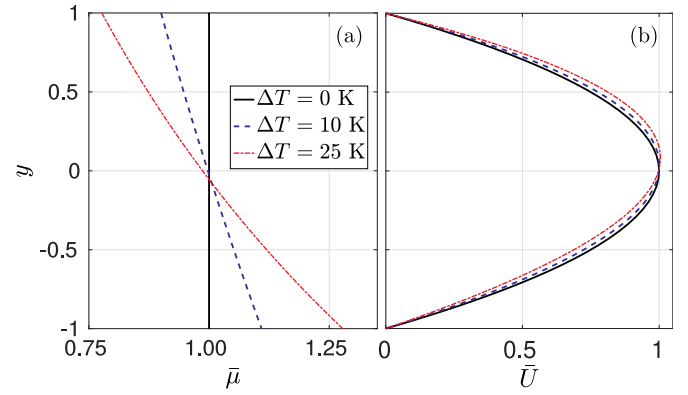


Fig. 3. Mean flow profiles (nondimensional) for different imposed temperature gradients. (a) Viscosity profile as given by the Arrhenius model for water, and (b) the corresponding mean velocity profile.

range of  $\Delta T$ , the discussion of the results is restricted to these values of  $\Delta T$  in the interest of brevity. In Fig. 4, the optimal perturbation characteristics are plotted as a function of  $Ri$ .

In Fig. 4(a), regardless of the value of  $\Delta T$  chosen, we show that the optimal transient growth  $G_{\max}$  decreases with increase in  $Ri$ . This can be attributed to stable stratification inhibiting strong vertical motion. On the other hand, as the viscosity difference between the two walls becomes larger,  $G_{\max}$  increases for a given  $Ri$ . We report that the increase in optimal growth is much more prominent at larger values of  $\Delta T$ . When comparing with the case  $\Delta T = 0 \text{ K}$ , there is about 60% increase in  $G_{\max}$  for  $Ri = 0.001$  when  $\Delta T = 80 \text{ K}$ . However, the change is not as drastic when  $\Delta T$  is lower; at  $\Delta T = 25 \text{ K}$ , the increase in  $G_{\max}$  ranges from 4% to 13% as  $Ri$  is varied. For the values of  $\Delta T$  chosen, the values of optimal transient growth  $G_{\max}$  are shown not to vary significantly when the fluid has non-constant viscosity.

The optimal time  $T_{opt}$ , as shown in Fig. 4(b), generally decreases with increasing strength of density stratification, and does not change markedly with  $\Delta T$ . For a wide range of values of  $Ri$ , the optimal disturbances are streamwise-independent, with  $\alpha_{opt} = 0$  (Fig. 4(c)). As the strength of the density stratification increases, we now find the optimal perturbations to be oblique, with  $\alpha_{opt} \neq 0$ . In Fig. 4(d), on increasing  $\Delta T$ , we see the spanwise wavenumber of the optimal perturbations  $\beta_{opt}$  taking on larger values. This directly translates to the perturbation structure becoming finer with smaller length scales. At  $Ri \approx 0.004$ , the kink in the  $T_{opt}$  curves corresponds to a new optimal perturbation emerging with a different optimal spanwise wavenumber  $\beta_{opt}$ . In this range of  $Ri$ , there exist multiple perturbations having different wavenumbers yielding very similar transient growth, but over different optimising times.

The values of  $G_{\max}$  suggest that sub-critical transition is a strong possibility in such systems for a range of values in  $Ri$ . Jerome et al. (2012) demonstrated using a simplified model that the lift-up mechanism is still largely responsible for the transient growth of perturbations, with the temperature perturbations serving as corrections. When the optimal perturbation is streamwise independent, the transient growth of perturbation energy is driven primarily by the lift-up mechanism (Landahl, 1980; Brandt, 2014). For oblique optimal perturbations, the energy amplification would be a combination of the Orr mechanism and the lift-up mechanism. However the corresponding  $G_{\max}$  values may be too low to cause transition of the flow.

The total perturbation energy (TE), as given by Eq. (14), has two contributions – the kinetic energy (KE) and the potential energy (PE). In Fig. 5(a), we report the PE contribution to the total (TE) at the initial time as a function of  $Ri$ ; note that, at  $t = 0$ , TE = 1. The potential energy is seen to account for more than 90% of the initial perturbation energy for a significant range of  $Ri$ . This suggests that the optimal perturbations are driven by buoyancy during the early stages of their evolution

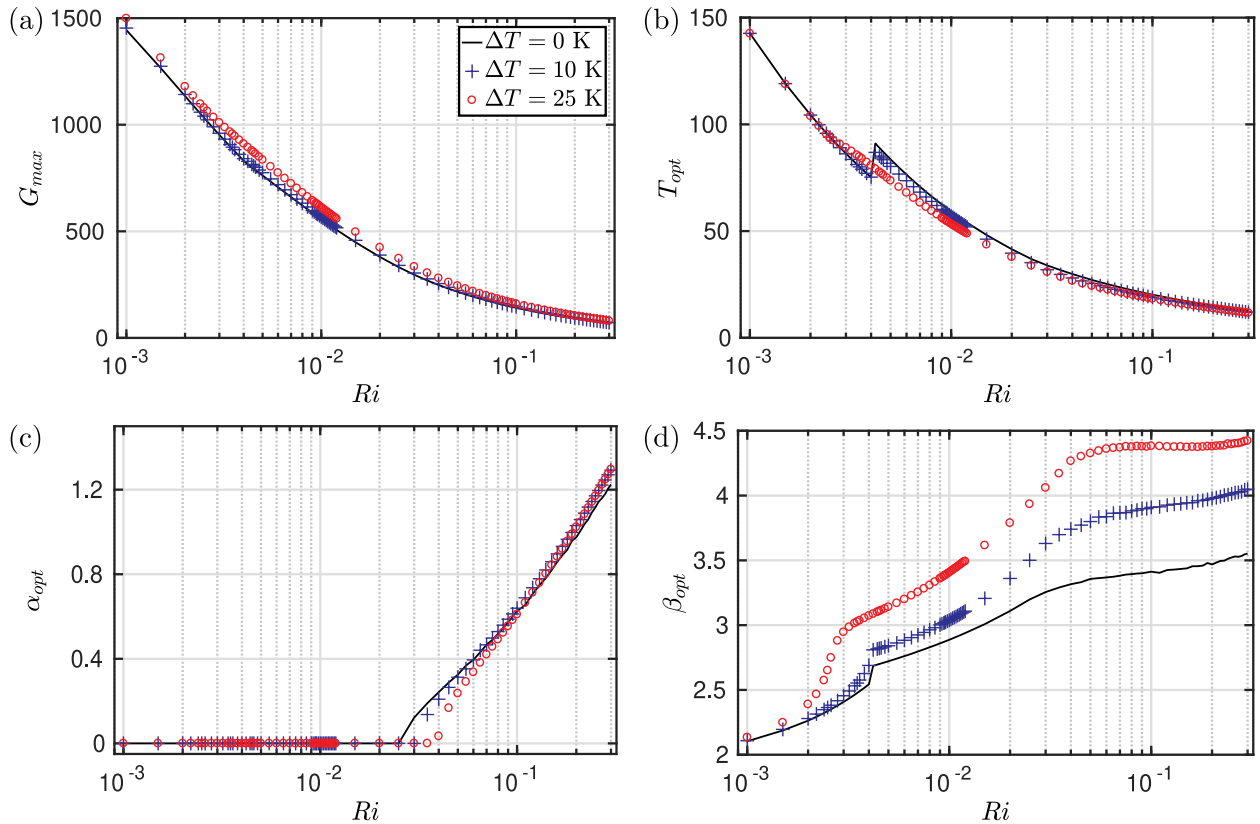


Fig. 4. Characteristics of the optimal perturbation for different  $\Delta T$ : (a) optimal transient growth  $G_{\max}$ , (b) optimal time  $T_{opt}$ , (c) optimal streamwise wavenumber  $\alpha_{opt}$ , (d) optimal spanwise wavenumber  $\beta_{opt}$ . Viscosity defined by Arrhenius model for water.

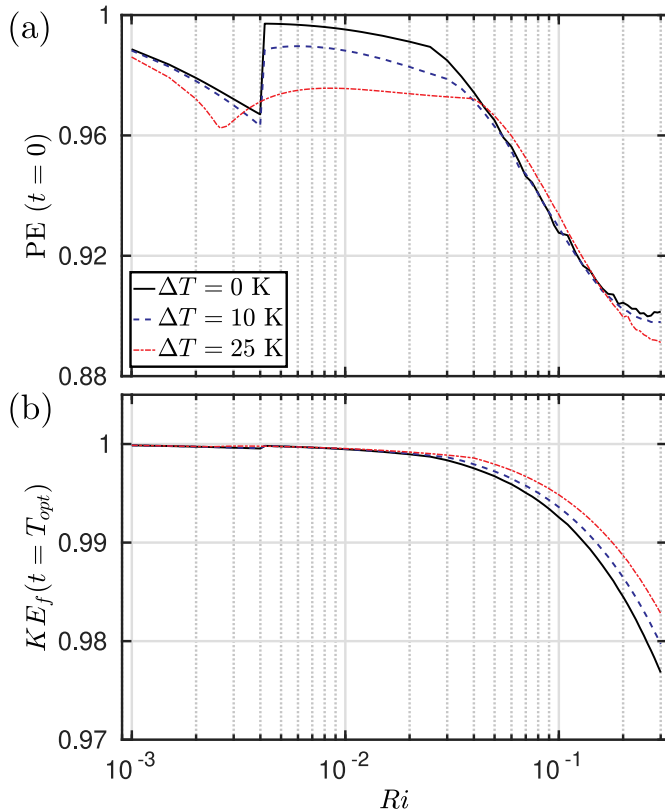


Fig. 5. Perturbation energy contributions. (a) At  $t = 0$ , PE. (b) At  $t = T_{opt}$ ,  $KE_f$  ( $= KE/TE$ ). Viscosity defined by Arrhenius model for water.

(see also Jose et al., 2015; 2018). At the optimal time, see Fig. 5(b), we instead display the fraction of total energy ( $KE_f = KE/TE$ ) that is due to the kinetic energy of the fluid motion. The figure clearly indicates that the TE is almost entirely due to the KE contribution at later stages of the perturbation evolution. This is consistent with the fact that the lift-up mechanism is dominant even in flows with temperature/density fluctuations (Jerome et al., 2012).

#### 4.2. Structure of optimal perturbations

In the previous subsection, it was shown that the optimal growth  $G_{\max}$  does not change significantly with the introduction of variable viscosity effects. However this does not shed light on the structure of the optimal perturbation as  $G_{\max}$  is a volume averaged quantity. From the trends shown by the optimal wavenumbers, we can expect changes in the perturbation structure. In the case of uniform viscosity, the optimal perturbations have symmetry about the channel centreline (for e.g. see Fig. 2 in Brandt, 2014). Here, we take a closer look at the structure of the optimal perturbations in the variable viscosity channel flow.

From the visualisation in Fig. 6, one can immediately see the effect of variable viscosity on the optimal perturbation structure. Fairly strong localisation is seen in the regions where the viscosity of the fluid is lower than the average viscosity in the channel. In such regions, vortical structures would persist for a longer period of time. Hence an initial perturbation that has its energy concentrated in the low viscosity region can be expected to be more efficient in driving the system towards transition. The perturbation energy does not redistribute to other regions in the channel in time in the linearised setting that governs the disturbance evolution here. However this points to the existence of a stronger localised streak at the optimal time as the overall optimal transient growth for the variable and the constant viscosity cases do not differ greatly. Therefore the fact that the two channel halves have

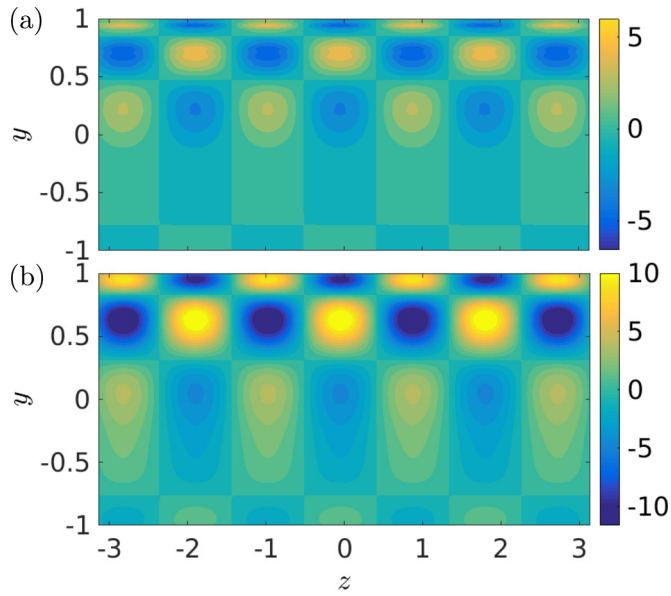


Fig. 6. Optimal perturbation at (a)  $t = 0$  and (b)  $t = T_{opt}$  when  $Ri = 0.01$ ,  $\Delta T = 25$  K. The colour denotes streamwise vorticity. Optimal perturbation characteristics:  $\alpha_{opt} = 0$ ,  $\beta_{opt} = 3.4058$ ,  $T_{opt} = 53.4036$ ,  $G_{max} = 612.7978$ . Viscosity defined by Arrhenius model for water.

different effective bulk Reynolds number finally emerges in the form of localisation of the optimal perturbation.

Following the above discussion, it is clear that a measure would be desirable to quantify how much of the perturbation energy is localised within a specific region of the channel. To define this specific region, there are innumerable options. Here we choose to divide the channel into two equal halves at the centreline, with one half having a lower average viscosity than the other. We define  $TE_{\mu_{<}}$  as the fraction of perturbation energy in the low viscosity half of the channel. In Fig. 7, we plot the values of  $TE_{\mu_{<}}$  at initial and optimal times as a function of  $Ri$ . Note that when  $\Delta T = 0$  K, the optimal perturbations are symmetric about the channel centreline as  $TE_{\mu_{<}} = 0.5$  for all values of  $Ri$ . With increase in viscosity stratification, it is seen that the fraction of perturbation energy in the low viscosity half becomes larger. In addition, there is negligible difference between these values at the initial and final times for the two values of  $\Delta T$  considered. The localisation appears to become stronger as the effect of the background stratification increases in strength. The channel can also be divided at the point  $y = y_m$ , where the velocity of the mean flow is maximum. An analysis of the distribution of perturbation energy in the sub-channels so formed also show similar trends as discussed above. The sub-channel with the lower average viscosity accounts for the greater proportion of the perturbation energy.

To get a better appreciation of what the localisation implies to the perturbation dynamics, we compare the optimal perturbation evolution to that of a mirrored initial condition  $q_{mir}$  while fixing the steady base state. The mirrored initial condition is simply a reflection of the optimal perturbation about the channel centreline, and is defined as  $q_{mir}(y) = q_{opt}(-y)$ . Therefore when the optimal perturbation has greater energy in one half of the channel for the viscosity stratified system, the mirrored initial condition will have more energy in the other half of the channel. For analysing the linear evolutions of different initial conditions, we examine how the perturbation energy (TE) and their distribution in the less viscous half ( $TE_{\mu_{<}}$ ) changes with time. It must be noted that the mirrored initial condition will not allow for the perturbation to attain the same peak in TE as the optimal perturbation.

When the localisation of the optimal perturbation is not very prominent, as is the case with  $Ri \approx 0.001$  (see Fig. 7), there are no significant differences in the peak values of TE. In Fig. 8(a), with  $Ri = 0.01$ ,

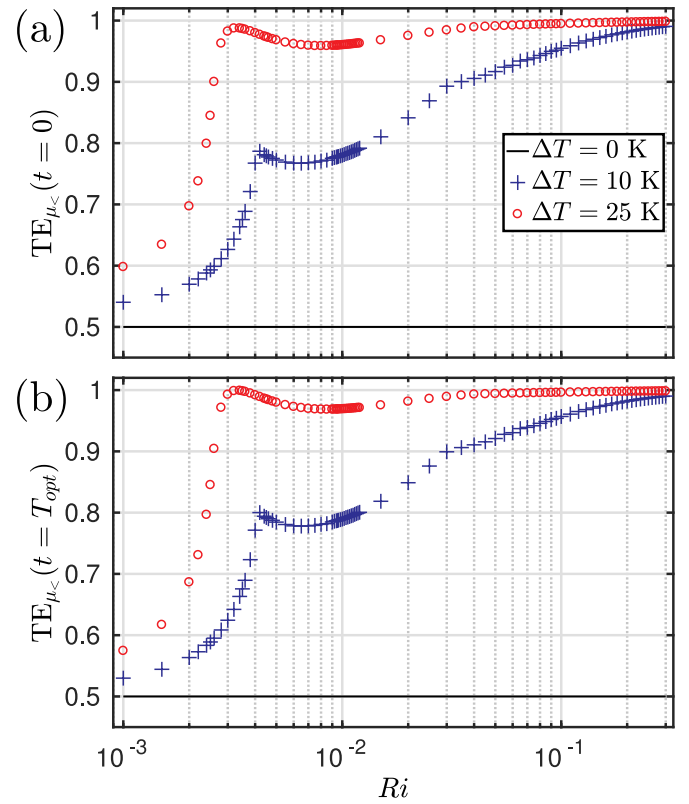


Fig. 7. Fraction of perturbation energy in less viscous half ( $TE_{\mu_{<}}$ ) for optimal perturbation as a function of  $Ri$  for different values of  $\Delta T$  at (a)  $t = 0$  and (b)  $t = T_{opt}$ . Note that, when  $\Delta T = 0$  K,  $TE_{\mu_{<}} = 0.5$  for all values of  $Ri$  at both  $t = 0$  and  $t = T_{opt}$ . Viscosity defined by Arrhenius model for water.

we present a case where the peak values of TE obtained are noticeably different. This difference becomes more pronounced with a stronger localisation of the optimal perturbation. The time evolution of the perturbation energy in the channel half of lowest base-flow viscosity,  $TE_{\mu_{<}}$  is displayed in Fig. 8(b) for different initial conditions. If  $TE_{\mu_{<}}$  is either lesser than or greater than 0.5, depending on the initial condition, it continues to be as such during the entire period of transient growth. This is due to the fact the dynamics under consideration is restricted to be linear. The inclusion of nonlinear effects might have significant bearing on this feature, as can be surmised from the findings of earlier studies on turbulent flows (for e.g. see Zonta et al., 2012a; 2012b).

## 5. Viscosity stratification in air

In this section, we consider the working fluid to be air whose viscosity is modelled by Sutherland's law (Sutherland, 1893):

$$\bar{\mu}_d = C_a \frac{\bar{T}_d^{3/2}}{\bar{T}_d + S},$$

$$\text{where } C_a = \frac{\mu_{ref}}{T_{ref}^{3/2}} (T_{ref} + S). \quad (16)$$

In the above,  $T_{ref} = 273.15$  K,  $S = 110.4$  K and  $\mu_{ref} = 1.716 \times 10^{-5}$  Nsm<sup>-2</sup>; this gives us  $C_a = 1.458 \times 10^{-6}$  kg/ms $\sqrt{K}$ . In contrast to the case with water, the viscosity of air is greater at higher temperatures. Consequently, as the upper wall is at a higher temperature, the upper half of the channel is more viscous. This translates to the average velocity in the lower half being greater than in the upper half. However, it should be noted that, for a given temperature difference between the walls, the change of the viscosity of air is not as pronounced as in water. For instance, when  $\Delta T = 25$  K, the ratio of the

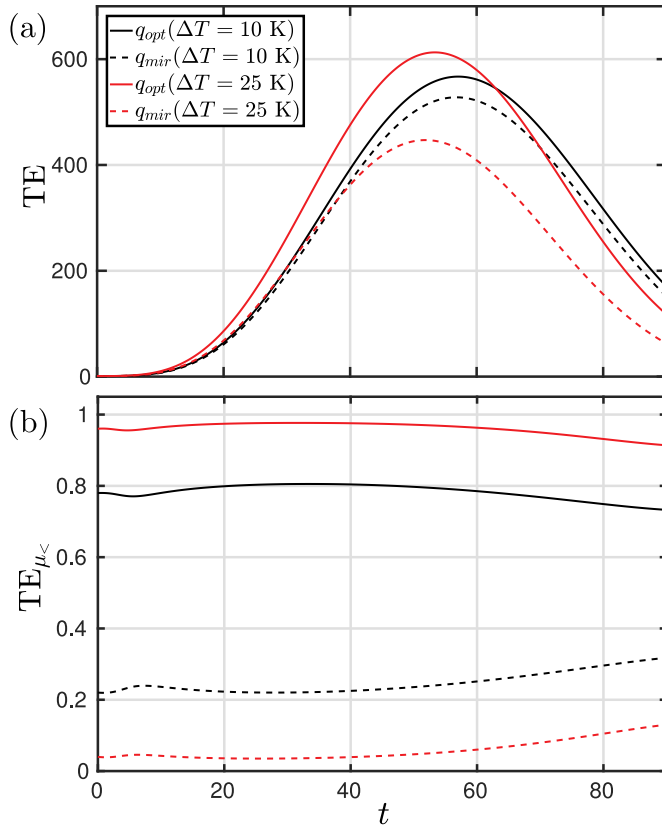


**Fig. 8.** (a) Evolution of the total perturbation energy  $TE$  for different initial conditions. (b) Evolution of perturbation energy fraction in the channel half of lowest viscosity  $TE_{\mu_{<}}$  as a function of time for different initial conditions. Viscosity defined by Arrhenius model for water.

maximum viscosity to minimum viscosity is 1.0642 when Sutherland's law is used; for the same  $\Delta T$ , this ratio is 1.6452 when the viscosity is defined by the Arrhenius model in Eq. (15); the effective bulk Reynolds number is 2605.47 and 2729.79 for the upper and lower halves respectively. Therefore the viscosity stratification can be deemed as weak in air.

For evaluating the optimal perturbations, we use  $Re = 2000$  and  $Pr = 1$ . As before, the flow is linearly stable for this choice of the governing parameters. To keep the focus on the localisation of the optimal perturbations, the nonmodal stability characteristics are provided in Appendix B. Here, we only state that the variation in the optimal transient growth  $G_{max}$  for the values of  $\Delta T$  selected is not significant. As discussed above, considering the small variations of  $G_{max}$ , one might be tempted to not consider variable viscosity effects in the analysis.

With regard to the structure of the optimal perturbations, we find a clear localisation due to viscosity stratification. In Fig. 9(a), we show the optimal perturbation to be more pronounced in the less viscous (lower) half of the channel. Once again, this points to a stronger streak in the less viscous half of the channel at the time when the perturbation energy is maximum. In Fig. 9(b), we plot the fraction of perturbation energy  $TE_{\mu_{<}}$  in the less viscous half as a function of  $Ri$  for different values of  $\Delta T$  at  $t = T_{opt}$ . At  $t = 0$ , the variation of  $TE_{\mu_{<}}$  of the optimal perturbations with  $Ri$  is very similar. For the cases with variable viscosity, as  $TE_{\mu_{<}}$  is greater than 0.5, the optimal perturbations are asymmetric about the channel centreline. The results presented in this section show that the localisation of optimal perturbations due to viscosity stratification is not an artefact of the viscosity model selected.

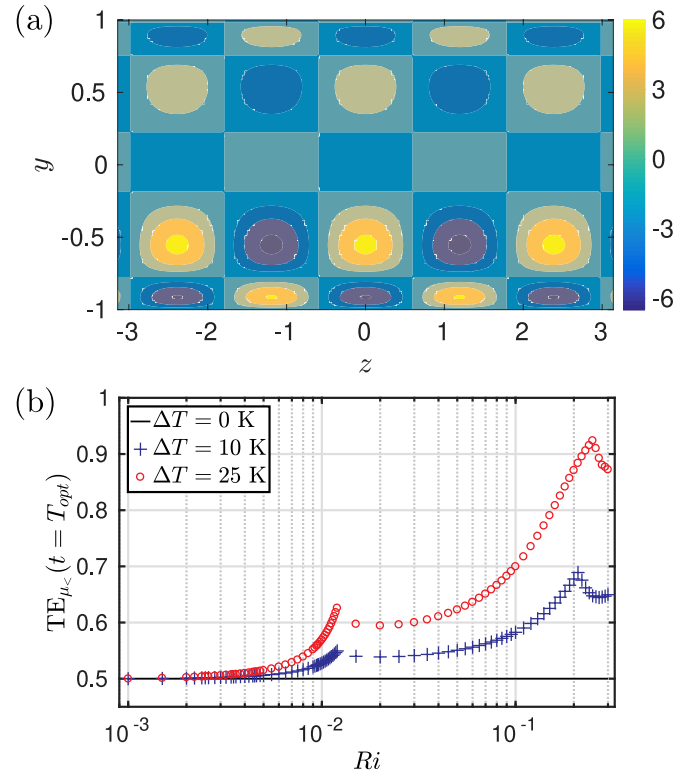


**Fig. 9.** Viscosity modelled by Sutherland's law. (a) Optimal perturbation at  $t = T_{opt}$  when  $Ri = 0.01$ ,  $\Delta T = 50 \text{ K}$ . The colour denotes streamwise vorticity. Optimal perturbation characteristics:  $\alpha_{opt} = 0$ ,  $\beta_{opt} = 2.6333$ ,  $T_{opt} = 48.2784$ ,  $G_{max} = 437.9821$ . (b) Fraction of perturbation energy in less viscous half ( $TE_{\mu_{<}}$ ) for optimal perturbation as a function of  $Ri$  for different values of  $\Delta T$  at  $t = T_{opt}$ . Note that, when  $\Delta T = 0 \text{ K}$ ,  $TE_{\mu_{<}} = 0.5$  for all values of  $Ri$ .

## 6. Conclusion

In this article, the nonmodal characteristics of a pressure driven channel flow with variable fluid viscosity have been discussed. We have considered two models for defining viscosity: Arrhenius model for water and Sutherland's law for air. For a large range of Richardson number, the optimal transient growth obtained is found to be significant regardless of the strength of the viscosity stratification, and therefore subcritical mechanisms can be considered strong candidates for causing the transition of the flow. However the difference in the optimal gain obtained despite including variable viscosity is not very drastic. On the other hand, we have shown that variable viscosity effects have strong implications on the structure of the optimal perturbation. The perturbation energy is found to be localised in regions where the fluid viscosity is lower. The localisation features survive throughout the linear evolution of the perturbation, and one therefore obtains strongly localised streaks in the system. On neglecting variable viscosity, we show that the localisation features are entirely missed. Such features are expected to have a significant bearing on the transition in these systems. A full nonlinear analysis of such transiently growing, localised optimals is required to get a more complete picture of the distribution of secondary fluid motions and eventually transition to turbulence. Therefore we conclude that judicious considerations must be taken before a choice can be made regarding whether variable viscosity can be neglected or not.

## CRedit authorship contribution statement

**Sharath Jose:** Conceptualization, Methodology, Formal analysis, Investigation, Writing - original draft. **Luca Brandt:** Conceptualization,

Methodology, Writing - review & editing. **Rama Govindarajan:** Conceptualization, Methodology, Writing - review & editing.

## Acknowledgments

LB acknowledges financial support from the Swedish Research Council Grant No. VR 2014-5001. RG acknowledges support of the Department of Atomic Energy, Government of India, under project no. 12-R&D-TFR-5.10-1100. The authors also wish to thank the anonymous referees for their suggestions.

## Declaration of Competing Interest

The authors declare that they have no known competing financial interests or personal relationships that could have appeared to influence the work reported in this paper.

## Appendix A. Derivation of laminar base flow

Here, we present the derivation of the mean flow when the viscosity is a function of the normal coordinate  $y$ . Under steady state conditions, the streamwise momentum equation reduces to:

$$0 = -\mathcal{G} + \frac{d}{dy} \left( \bar{\mu} \frac{dU}{dy} \right). \quad (17)$$

Above,  $\mathcal{G}$  is the nondimensional mean pressure gradient in the streamwise direction. Integrating once, we get:

$$\mathcal{G}y + C_1 = \bar{\mu} \frac{dU}{dy} \quad (18)$$

Above,  $C_1$  is the constant of integration. Integrating again, we get:

$$U(y) = \mathcal{G} \int_{-1}^y dy' \frac{y'}{\bar{\mu}(y')} + C_1 \int_{-1}^y dy' \frac{1}{\bar{\mu}(y')} + C_2 \quad (19)$$

Above,  $C_2$  is another constant of integration. The mean flow obeys no-slip boundary conditions at the walls, i.e.,  $U(\pm 1) = 0$ . As a consequence,  $C_2 = U(-1) = 0$ . Using the boundary condition at the upper wall, we get:

$$\frac{C_1}{\mathcal{G}} = -\frac{I_2}{I_1}$$

$$\text{where } I_1 = \int_{-1}^1 dy' \frac{1}{\bar{\mu}(y')} \text{ and } I_2 = \int_{-1}^1 dy' \frac{y'}{\bar{\mu}(y')}. \quad (20)$$

As the viscosity is not constant across the channel,  $U$  is no longer symmetric about the channel centreline. Let  $U_m$  be the maximum velocity at  $y = y_m$ ; typically we choose  $U_m = 1$  for simplicity. As the RHS of Eq. (18) goes to zero at  $y = y_m$ , we get:

$$y_m = -\frac{C_1}{\mathcal{G}} = \frac{I_2}{I_1}. \quad (21)$$

Note that  $y_m$  depends only on the viscosity profile. When the fluid viscosity is constant, it can be readily verified that  $y_m = 0$ , i.e., the channel centreline.

As  $U(y_m) = U_m$ , using Eqs. (19) and (20), we can derive expressions for  $\mathcal{G}$  and  $C_1$  as follows:

$$\mathcal{G} = \frac{U_m I_1}{I_1 I_2' - I_2 I_1'} \quad (22)$$

$$C_1 = -\frac{U_m I_2}{I_1 I_2' - I_2 I_1'}$$

$$\text{where } I_1' = \int_{-1}^{y_m} dy' \frac{1}{\bar{\mu}(y')} \text{ and } I_2' = \int_{-1}^{y_m} dy' \frac{y'}{\bar{\mu}(y')}. \quad (23)$$

Finally, the mean flow is obtained as follows:

$$U(y) = \frac{U_m}{I_1 I_2' - I_2 I_1'} \left[ I_1 \int_{-1}^y dy' \frac{y'}{\bar{\mu}(y')} - I_2 \int_{-1}^y dy' \frac{1}{\bar{\mu}(y')} \right]. \quad (24)$$

When the viscosity is constant ( $\bar{\mu} = 1$ ), it can be verified that the familiar parabolic profile that is symmetric about the centreline is obtained.

## Appendix B. Optimal perturbation characteristics for air

With the viscosity of air modelled by Sutherland's law, Fig. 10 shows the optimal transient growth characteristics as a function of  $Ri$  for different  $\Delta T$ . We note insignificant changes in the optimal transient growth, which also holds true for the other features of the optimal perturbation such as the optimal time  $T_{opt}$  when the disturbance attains its maximum energy. For a wide range of  $Ri$ , the optimal perturbations are streamwise independent, i.e.,  $\alpha_{opt} = 0$ . Unlike for the results obtained with the Arrhenius model, the optimal spanwise wavenumber  $\beta_{opt}$  does not change considerably. It is to be noted that variations of  $\beta_{opt}$  with viscosity stratification offers a preliminary clue about the structure of the optimal perturbation. Furthermore, we confirm that the early time dynamics is buoyancy driven before momentum forcing takes over at later times.

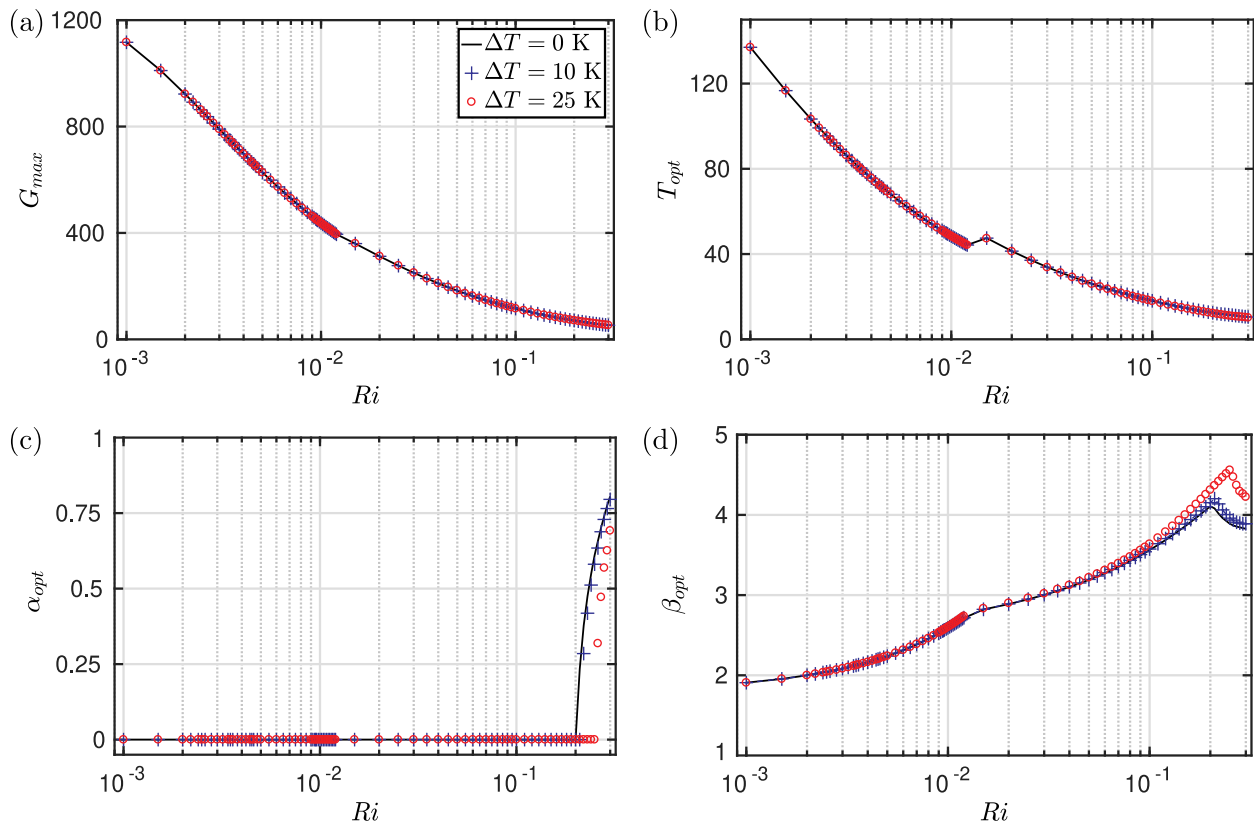


Fig. 10. Viscosity modelled by Sutherland's law. Characteristics of the optimal perturbation for different  $\Delta T$ : (a) optimal transient growth  $G_{max}$ , (b) optimal time  $T_{opt}$ , (c) optimal streamwise wavenumber  $\alpha_{opt}$ , (d) optimal spanwise wavenumber  $\beta_{opt}$ .

## References

- Brandt, L., 2014. The lift-up effect: The linear mechanism behind transition and turbulence in shear flows. *Eur. J. Mech. B Fluids* 47, 80–96.
- Chikkadi, V., Sameen, A., Govindarajan, R., 2005. Preventing Transition to Turbulence: A Viscosity Stratification Does Not Always Help. *Phys. Rev. Lett.* 95 (26), 264504.
- Drazin, P.G., Reid, W.H., 2004. *Hydrodynamic Stability*. Cambridge University Press.
- Gad-el-Hak, M., 2001. *Flow Control: Passive, Active, and Reactive Flow Management*. Cambridge University Press.
- Govindarajan, R., L'vov, V.S., Procaccia, I., 2001. Retardation of the onset of turbulence by minor viscosity contrasts. *Phys. Rev. Lett.* 87 (17), 174501.
- Govindarajan, R., Sahu, K.C., 2014. Instabilities in viscosity-stratified flow. *Annu. Rev. Fluid Mech.* 46, 331–353.
- Jerome, J.S., Chomaz, J.M., Huerre, P., 2012. Transient growth in Rayleigh-Bénard-Poiseuille/Couette convection. *Phys. Fluids* 24, 044103–1–27.
- Jose, S., Roy, A., Bale, R., Govindarajan, R., 2015. Analytical solutions for algebraic growth of disturbances in a stably stratified shear flow. *Proc. R. Soc. A* 471 (2181), 20150267.
- Jose, S., Roy, A., Bale, R., Iyer, K., Govindarajan, R., 2018. Optimal energy growth in a stably stratified shear flow. *Fluid Dyn. Res.* 50 (1), 011421.
- Kaminski, A.K., Caulfield, C.P., Taylor, J.R., 2014. Transient growth in strongly stratified shear layers. *J. Fluid Mech.* 758, R4.
- Landahl, M.T., 1980. A note on an algebraic instability of inviscid parallel shear flows. *J. Fluid Mech.* 98, 243–251.
- Lee, J., Jung, S.Y., Sung, H.J., Zaki, T.A., 2013. Effect of wall heating on turbulent boundary layers with temperature-dependent viscosity. *J. Fluid Mech.* 726, 196–225.
- Lee, J., Jung, S.Y., Sung, H.J., Zaki, T.A., 2014. Turbulent thermal boundary layers with temperature-dependent viscosity. *Int. J. Heat Fluid Flow* 49, 43–52.
- Nouar, C., Bottaro, A., Brancher, J.P., 2007. Delaying transition to turbulence in channel flow: revisiting the stability of shear-thinning fluids. *J. Fluid Mech.* 592, 177–194.
- Pecnik, R., Patel, A., 2017. Scaling and modelling of turbulence in variable property channel flows. *J. Fluid Mech.* 823, R1.
- Ranganathan, B.T., Govindarajan, R., 2001. Stabilization and destabilization of channel flow by location of viscosity-stratified fluid layer. *Phys. Fluids* 13 (1), 1–3.
- Ren, J., Fu, S., Pecnik, R., 2019. Linear instability of Poiseuille flows with highly non-ideal fluids. *J. Fluid Mech.* 859, 89–125.
- Sameen, A., Bale, R., Govindarajan, R., 2011. The effect of wall heating on instability of channel flow - corrigendum. *J. Fluid Mech.* 673, 603–605.
- Sameen, A., Govindarajan, R., 2007. The effect of wall heating on instability of channel flow. *J. Fluid Mech.* 577, 417–442.
- Schmid, P.J., 2007. Nonmodal stability theory. *Annu. Rev. Fluid Mech.* 39, 129–162.
- Schmid, P.J., Brandt, L., 2014. *Analysis of Fluid Systems: Stability, Receptivity, Sensitivity*. Lecture notes from the FLOW-NORDITA Summer School on Advanced Instability Methods for Complex Flows, Stockholm, Sweden, 2013. *Appl. Mech. Rev.* 66 (2), 24803.
- Schmid, P.J., Henningson, D.S., 2001. *Stability and Transition in Shear Flows*. Springer-Verlag.
- Sutherland, W., 1893. LII. The viscosity of gases and molecular force. *Phil. Mag.* 36 (223), 507–531.
- Taguelmimt, N., Danaila, L., Hadjadj, A., 2016. Effect of viscosity gradients on mean velocity profile in temporal mixing layer. *J. Turbul.* 17 (5), 491–517.
- Talbot, B., Danaila, L., Renou, B., 2013. Variable-viscosity mixing in the very near field of a round jet. *Phys. Scripta* 2013 (T155), 014006.
- Voivenel, L., Danaila, L., Varea, E., Renou, B., Cazalens, M., 2016. On the similarity of variable viscosity flows. *Phys. Scripta* 91 (8), 084007.
- Wall, D.P., Wilson, S.K., 1996. The linear stability of channel flow of fluid with temperature-dependent viscosity. *J. Fluid Mech.* 323, 107–132.
- Weideman, J.A., Reddy, S.C., 2000. A MATLAB differentiation matrix suite. *ACM Trans. Math. Softw.* 26, 465–519.
- White, C.M., Mungal, M.G., 2008. *Mechanics and prediction of turbulent drag reduction with polymer additives*. *Annu. Rev. Fluid Mech.* 40, 235–256.
- Yih, C.-S., 1967. Instability due to viscosity stratification. *J. Fluid Mech.* 27 (02), 337–352.
- Zonta, F., 2013. Nusselt number and friction factor in thermally stratified turbulent channel flow under non-Oberbeck-Boussinesq conditions. *Int. J. Heat Fluid Flow* 44, 489–494.
- Zonta, F., Marchioli, C., Soldati, A., 2012a. Modulation of turbulence in forced convection by temperature-dependent viscosity. *J. Fluid Mech.* 697, 150–174.
- Zonta, F., Onorato, M., Soldati, A., 2012b. Turbulence and internal waves in stably-stratified channel flow with temperature-dependent fluid properties. *J. Fluid Mech.* 697, 175–203.